Article

Not peer-reviewed version

A 33 GHz Conformal Phased-Array Radar with Linearly Constrained Minimum Variance Digital Beamforming, Circular-Polarization Filtering, and Neural-Network Micro-Doppler Classification for Counter-UAS Applications

Michael Baginski *

Posted Date: 23 March 2026

doi: 10.20944/preprints202603.1736.v1

Keywords: millimeter-wave radar; conformal phased array; LCMV beamforming; digital beamform-ing; RHCP; circular polarization; micro-Doppler; neural network; Ka-band; counter-UAS; detect-and-avoid

 doi:10.20944/preprints202603.1736.v1

Article

A 33 GHz Conformal Phased-Array Radar with Linearly Constrained Minimum Variance Digital Beamforming, Circular-Polarization Filtering, and Neural-Network Micro-Doppler Classification for Counter-UAS Applications

Michael Baginski

Department of Electrical and Computer Engineering, Auburn University, Auburn, AL 36849, USA; baginme@auburn.edu; Tel.: +1-334-844-1817

Abstract

A compact millimeter-wave radar system operating at 33 GHz is presented for integration on small unmanned aerial systems (UAS) and for ground-based counter-UAS reconnaissance. The system is based on a 36-element hemispherical conformal phased array of crossed half-wave dipole radiators that generates right-hand circular polarization (RHCP) on transmit and selectively receives left-hand circular polarization (LHCP) echoes from targets, providing passive first-stage suppression of co-polarized rain and ground clutter. A Linearly Constrained Minimum Variance (LCMV) digital beamformer, applied to per-element analog-to-digital converter (ADC) outputs, delivers closed-form beam weights that enforce a distortionless response at each scan direction while globally minimizing sidelobe power. The formulation resolves the main-beam drift caused by the ill-conditioned re-scaling step in iterative Chebyshev tapering, achieving sidelobe levels below -20 dB with main-beam peaks within 0.1° of their commanded angles across all evaluated positions. Mutual coupling between array elements is modeled analytically using the induced-EMF method, yielding a 36×36 impedance matrix whose off-diagonal entries are at most 8.2% of the element self-impedance at the minimum inter-element separation of 2.70 λ. A closed-form decoupling matrix is applied to the receive manifold prior to LCMV weight computation, and the resulting coupling-corrected and uncoupled beam patterns are compared quantitatively. Seven simultaneous independent receive beams covering 0°–60° elevation are formed from a single data snapshot. A Scaled Conjugate Gradient neural network classifier, trained on radar-equation-scaled micro-Doppler features following Swerling I–IV radar cross-section (RCS) fluctuation statistics, achieves overall classification accuracy above 85% across five target classes. The design methodology provides a complete end-to-end simulation framework spanning element modeling, beamformer synthesis, coherent link-budget analysis, and AI-based classification relevant to drone detect-and-avoid (DAA) and counter-UAS (C-UAS) applications.

Keywords: millimeter-wave radar; conformal phased array; LCMV beamforming; digital beamforming; RHCP; circular polarization; micro-Doppler; neural network; Ka-band; counter-UAS; detect-and-avoid

1. Introduction

The proliferation of commercial and recreational unmanned aerial vehicles (UAVs) in civil airspace presents growing challenges for air-traffic management, critical-infrastructure protection, and public safety [1,4]. Reliable detection, classification, and tracking of small UAVs require sensory systems that operate effectively under adverse weather conditions, at ranges beyond visual line of sight (BVLOS), and with low probability of confusion between drones and benign airspace users such as birds. Optical and electro-optical/infrared (EO/IR) systems provide high-resolution imagery but suffer

 doi:10.20944/preprints202603.1736.v1

significant performance degradation in fog, precipitation, and night conditions [2]. Acoustic sensors are limited to short-range scenarios and are susceptible to background noise from wind and urban environments. Radar sensing, by contrast, maintains reliable operation under all weather conditions, provides simultaneous range and velocity measurements, and scales naturally to the millimeter-wave (mmWave) frequency bands that enable compact aperture designs compatible with small drone platforms. These properties make radar the centerpiece of state-of-the-art detect-and-avoid (DAA) and counter-UAS (C-UAS) system architectures [1,2].

Recent research has focused on cognitive and adaptive radar architectures that dynamically manage sensing resources in dense, contested environments [1–3]. Phased-array implementations with electronic beam steering enable rapid revisit scheduling, simultaneous multi-target tracking, and reconfigurable spatial filtering without mechanical moving parts [5,8]. Conformal array geometries allow these capabilities to be integrated directly onto curved structural surfaces such as UAV fuselages, eliminating aerodynamic protrusions, reducing drag, and lowering the radar cross-section of the host platform [7,8].

The Ka-band frequency near 33 GHz offers a favorable combination of properties for compact airborne radar. The free-space wavelength $\lambda \approx 9.1$ mm enables sub-centimeter element spacing and aperture dimensions of a few centimeters for a 36-element array, while preserving sufficient spatial resolution for individual micro-Doppler feature discrimination. Atmospheric propagation losses at 33 GHz are moderate compared with higher Ka-band frequencies and are well characterized for the short- to medium-range regimes of 100–500 m relevant to DAA and C-UAS applications [6,11].

An additional advantage in the design presented is the use of circular polarization (CP). The transmission of right-hand circular polarization will be reflected as left-hand circular or elliptical polarization (LHCP, LHEP) from targets, whereas distributed clutter scatterers—rain, vegetation, and ground—predominantly preserve polarization handedness [11]. A radar that transmits RHCP and receives only LHCP therefore achieves a passive first stage of clutter suppression before any digital processing is applied, reducing ADC dynamic range requirements and improving the effective SNR at the beamformer input. Realizing this on a conformal surface requires careful analytical characterization of the element cross-polarization isolation (XPI) as a function of scan angle, which this work provides.

Target classification exploits micro-Doppler signatures arising from the time-varying motion of individual scattering centers [6]. Rotating propellers, flapping wings, and structural vibrations superimpose frequency modulations on the bulk Doppler return that are highly discriminative between drones, birds, and clutter. When combined with the spatial gain of a phased array and the coherent integration advantage of pulse-Doppler processing, micro-Doppler features provide a rich basis for neural-network classification even at low instantaneous signal-to-noise ratio (SNR).

The key contributions of this work are:

1. **Conformal CP array design.** A 36-element hemispherical phased array at 33 GHz using crossed half-wave dipoles, with analytical RHCP/LHCP element patterns and a closed-form expression for XPI versus elevation angle.
2. **LCMV beamforming.** A closed-form Linearly Constrained Minimum Variance (LCMV) solution enforcing a distortionless response in the scan direction while minimizing sidelobe power, eliminating the instability of iterative Chebyshev tapering for conformal arrays.
3. **Mutual coupling compensation.** An induced-EMF-based mutual impedance matrix for 630 element pairs and a closed-form decoupling matrix, $\mathbf{C} = Z_{\text{self}}\mathbf{Z}^{-1}$, applied to the receive manifold, with quantified sidelobe reduction over scan.
4. **Multi-beam operation.** Per-element time-delay alignment enabling seven simultaneous receive beams from a single ADC snapshot.
5. **Radar link budget.** A coherent SNR model relating transmit power, two-way array gain, Swerling RCS, and the Albersheim threshold to maximum range for representative small targets.

 doi:10.20944/preprints202603.1736.v1

6. **Micro-Doppler classification.** A Scaled Conjugate Gradient neural network trained on radar-scaled synthetic features, achieving $> 85\%$ accuracy across five Swerling classes under mixed SNR.

2. Radar System Architecture

The proposed system is a monostatic 33 GHz pulse-Doppler radar employing a 36-element hemispherical conformal phased array. Table 1 summarizes the key system parameters.

Table 1. Key radar system parameters.

Parameter	Symbol	Value
Carrier frequency	f_c	33 GHz (Ka-band)
Wavelength	λ	9.09 mm
Number of elements	N	36
Element type	—	Crossed $\lambda/2$ dipoles
Transmit polarization	—	RHCP
Receive polarization	—	LHCP
Dome radius	R_{dome}	83.2 mm (9.15λ)
Dipole half-length	ℓ	4.55 mm ($\lambda/2$)
Transmit power	P_t	50 mW
Pulse width	τ_p	1 μs
Noise bandwidth	B_n	1 MHz
Pulse repetition frequency	PRF	10 kHz
CPI duration	T_{CPI}	0.5 s
Pulses per CPI	N_p	5000
Per-element noise figure	NF	6 dB
System losses	L_s	3 dB
Aperture efficiency	η_a	0.75
Array directivity	G	18.6 dBi
Elevation scan coverage	—	0°–70°
Azimuth scan coverage	—	360° (full)
SLL design target	—	-20 dB
Beamformer type	—	LCMV (closed form)
Simultaneous receive beams	M	7

2.1. Array Geometry

Elements are distributed across the hemispherical dome surface in four concentric rings optimized for 0°–70° elevation scan coverage:

$$\text{Ring 0: 1 element at } \theta_n = 0^\circ; \quad \text{Ring 1: 5 at } 18^\circ; \quad \text{Ring 2: 12 at } 38^\circ; \quad \text{Ring 3: 18 at } 58^\circ. \tag{1}$$

The dome radius is set by requiring at least $\lambda/2$ arc-length spacing on the densest ring:

$$R_{\text{dome}} \geq \frac{N_3\,\lambda}{4\pi \sin\theta_3}, \tag{2}$$

where $N_3 = 18$ and $\theta_3 = 58^\circ$. Applying a 15% clearance factor and a minimum floor of 2.5λ gives $R_{\text{dome}} \approx 26$ mm at 33 GHz. Successive rings are azimuthally staggered by $180^\circ/N_r$ to improve the uniformity of the far-field aperture illumination. The resulting element distribution is illustrated in Figure 1.

 doi:10.20944/preprints202603.1736.v1

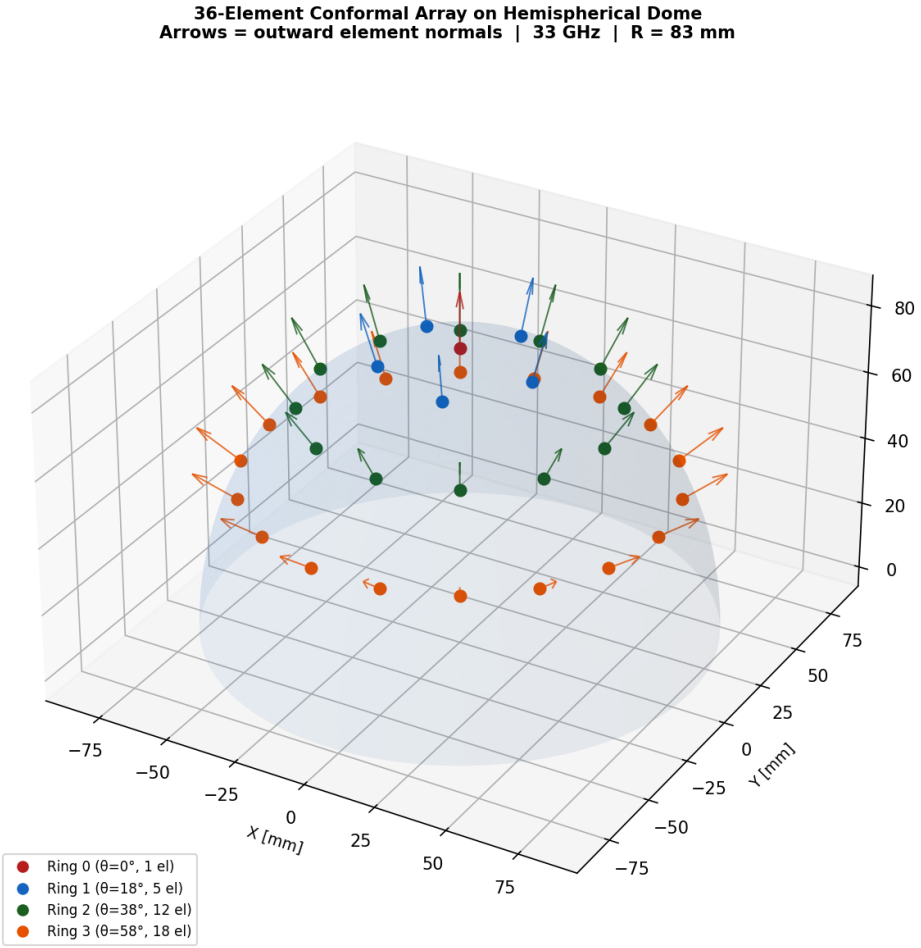

Figure 1. Distribution of the 36 crossed-dipole elements on the hemispherical conformal surface. Marker color encodes ring elevation angle (0°–58°). Arrows indicate outward surface normals used for local-angle element-pattern computation.

2.2. Digital Beamforming Receive Architecture

Each element feeds an independent receive chain comprising a low-noise amplifier (LNA), down-conversion mixer, and ADC. The $N \times 1$ complex baseband snapshot vector is

$$\mathbf{y}(t) = \mathbf{v}(\theta, \phi)\, s(t) + \mathbf{n}(t), \tag{3}$$

where $\mathbf{v}(\theta, \phi) \in \mathbb{C}^N$ is the array manifold vector, $s(t)$ is the target echo signal, and $\mathbf{n}(t) \sim \mathcal{CN}(\mathbf{0}, \sigma_n^2 \mathbf{I})$ is complex Gaussian thermal noise. The beamformer output for weight vector $\mathbf{w} \in \mathbb{C}^N$ is

$$z(t) = \mathbf{w}^H \mathbf{y}(t), \tag{4}$$

and the beamformed total radiated power (TRP) at observation direction (θ_i, ϕ_i) is

$$P(\theta_i, \phi_i) = \left| \mathbf{w}^H \mathbf{v}(\theta_i, \phi_i) \right|^2. \tag{5}$$

2.3. Radar Processing Chain

The overall radar architecture is shown in Figure 2. After waveform generation and RHCP transmission, echoes are simultaneously recorded at all 36 ADC outputs. LCMV digital beamforming focuses the receive aperture on the desired look direction. Range–Doppler processing over the CPI produces a two-dimensional amplitude map from which detections are declared using a constant-false-

 doi:10.20944/preprints202603.1736.v1

alarm-rate (CFAR) threshold. Micro-Doppler feature extraction and neural-network inference then classify detected returns.

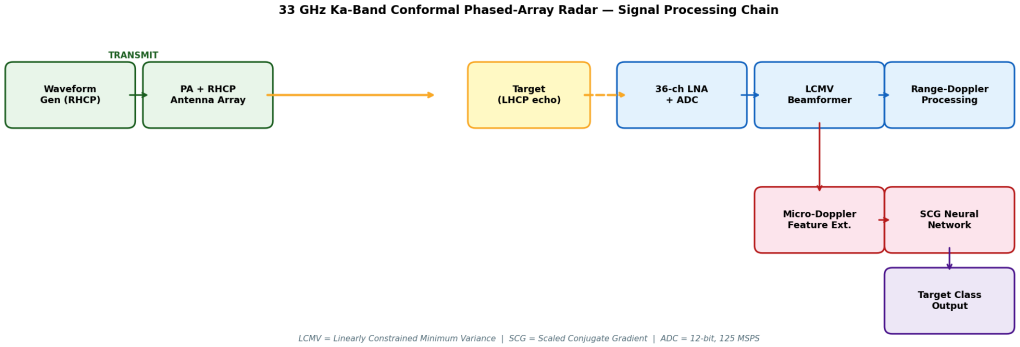

Figure 2. System block diagram. RF echoes enter 36 independent receive chains; LCMV digital beamforming forms the spatial beam; range–Doppler processing extracts bulk target motion; Hann-windowed Doppler spectra feed the neural-network classifier.

3. Crossed-Dipole Element Pattern and Polarization

3.1. Half-Wave Dipole Radiation Function

Each radiator consists of two orthogonal half-wave dipoles whose axes lie in the local surface-tangent plane at element n, directed along $\hat{x}'_n$ and $\hat{y}'_n$, and fed with equal amplitudes but a 90° phase offset.

Angle convention. In the standard treatment [9], the dipole lies along the z-axis and the polar angle θ_B is measured from that axis, so the pattern maximum is at $\theta_B = 90°$ and nulls occur at $\theta_B = 0°$ and 180°. In the conformal-array context it is more natural to define the local angle θ' from the outward element normal $\hat{n}_n$, which is perpendicular to the dipole axis. The two angles are therefore complementary: $\theta_B = 90° - \theta'$, so $\theta' = 0°$ is the boresight direction (maximum radiation toward $\hat{n}_n$) and $\theta' = 90°$ is the element null (along the dipole axis, in the surface tangent plane). Figure 3 illustrates this convention.

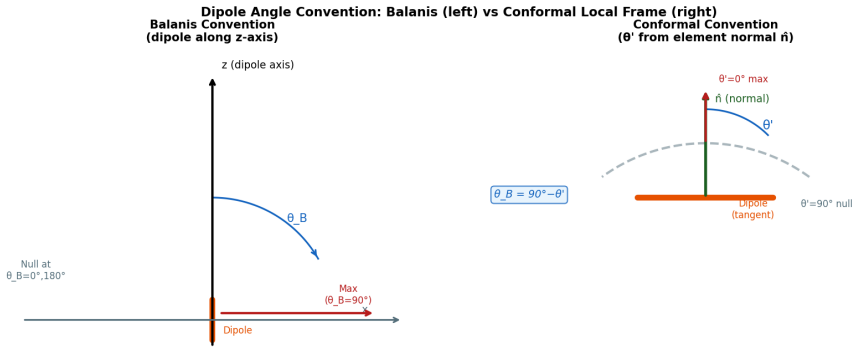

Figure 3. Angle convention for the conformal array element pattern. **Left:** Standard convention — dipole along z, polar angle θ_B measured from the dipole axis; maximum radiation at $\theta_B = 90°$, nulls at 0° and 180°. **Right:** Local conformal convention — θ' measured from the outward element normal $\hat{n}_n$; the dipole lies in the surface-tangent plane; maximum radiation at $\theta' = 0°$ (toward $\hat{n}_n$), null at $\theta' = 90°$. The two angles are related by $\theta_B = 90° - \theta'$.

Substituting $\theta_B = \pi/2 - \theta'$ into the standard half-wave dipole radiation function gives the element pattern in the local frame [9]:

$$F(\theta') = \begin{cases} \dfrac{\cos\left(\frac{\pi}{2}\sin\theta'\right)}{\cos\theta'}, & \theta' \neq \dfrac{\pi}{2}, \\ 0, & \theta' = \dfrac{\pi}{2}, \end{cases} \tag{6}$$

 doi:10.20944/preprints202603.1736.v1

where $\theta' \in [0, \pi/2]$ for elements facing the scan hemisphere.

3.2. RHCP and LHCP Power Patterns

In the element's local spherical frame (θ', ϕ'), the total far-field electric field from the quadrature-fed dipole pair is

$$\mathbf{E}(\theta', \phi') = F(\theta') \Big[(\cos\phi'\,\hat{\theta}' - \sin\phi'\,\hat{\phi}') + j(\sin\phi'\,\hat{\theta}' + \cos\phi'\,\hat{\phi}') \Big]. \tag{7}$$

Projecting onto the RHCP and LHCP circular-polarization basis vectors, the normalized power patterns are [9]

$$g_{\mathrm{RHCP}}(\theta') = \left[\frac{F(\theta')}{F(0)} \right]^2, \tag{8}$$

$$g_{\mathrm{LHCP}}(\theta') = \left[\frac{F(\theta') \sin\theta'}{F(0)} \right]^2. \tag{9}$$

3.3. Cross-Polarization Isolation

The cross-polarization isolation (XPI) is defined as

$$\mathrm{XPI}(\theta') = 10 \log_{10} \left[\frac{g_{\mathrm{RHCP}}(\theta')}{g_{\mathrm{LHCP}}(\theta')} \right] = -10 \log_{10}(\sin^2\theta'). \tag{10}$$

At boresight, XPI tends to infinity because the LHCP component vanishes exactly. At $\theta' = 70^\circ$ (the scan-volume edge), XPI ≈ 0.5 dB. The RHCP and LHCP power patterns and XPI versus elevation angle are shown in Figure 4.

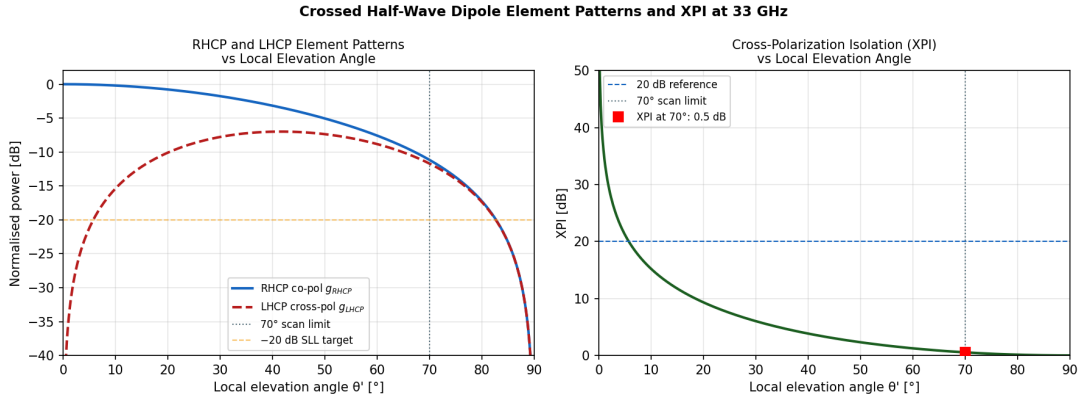

Figure 4. Crossed-dipole element patterns and cross-polarization isolation. **Left:** Normalized RHCP co-pol (solid) and LHCP cross-pol (dashed) power patterns versus local elevation angle θ'. The vertical dotted line marks the 70° scan-volume limit; the horizontal dashed line shows the -20 dB SLL target. **Right:** XPI versus θ'; the 20 dB reference level and the 0.5 dB minimum at 70° are indicated.

3.4. Array Manifold

The RHCP manifold vector at observation direction $\hat{k} = [\sin\theta\cos\phi,\ \sin\theta\sin\phi,\ \cos\theta]^\top$ is

$$\big[\mathbf{v}(\theta, \phi)\big]_n = \sqrt{g_{\mathrm{RHCP}}(\theta'_n)}\ \exp\!\big(jk_0\,\mathbf{r}_n \cdot \hat{k}\big), \quad n = 1, \ldots, N, \tag{11}$$

where $\theta'_n = \arccos(\hat{n}_n \cdot \hat{k})$ and $k_0 = 2\pi/\lambda$.

3.5. Mutual Coupling Model

The isolated-element manifold (11) omits inter-element coupling: in reality the terminal voltage at element n receives induced contributions from all other excited elements. This section derives the

 doi:10.20944/preprints202603.1736.v1

analytical mutual impedance matrix and the corresponding receive-manifold correction applied in all beam computations.

3.5.1. Impedance Matrix

The minimum inter-element separation in the array is 24.50 mm (outer ring, adjacent azimuthal neighbors at $\theta = 58°$), corresponding to 2.70 λ at 33 GHz. At this spacing the Balanis induced-EMF method [9] provides an accurate closed-form mutual impedance. For two half-wave dipoles m and n separated by distance d [9,12]:

$$Z_{mn} = \frac{\eta_0}{4\pi}\Big[2\,\mathrm{Ci}(kR_1) + 2\,\mathrm{Ci}(kR_2) - 4\,\mathrm{Ci}(kd) + j\big(2\,\mathrm{Si}(kR_1) + 2\,\mathrm{Si}(kR_2) - 4\,\mathrm{Si}(kd)\big)\Big]\cos\psi_{mn}, \quad (12)$$

where $\eta_0 = 376.73\ \Omega$, $k = 2\pi/\lambda$, $R_1 = \sqrt{d^2 + (L/2)^2} + L/2$, $R_2 = |\sqrt{d^2 + (L/2)^2} - L/2|$, $L = \lambda/2$, $\mathrm{Ci}(\cdot)$ and $\mathrm{Si}(\cdot)$ are the cosine and sine integrals, and $\cos\psi_{mn}$ is the dot product of the local $\hat{\theta}'$-axis unit vectors of elements m and n. The diagonal entries are the classical half-wave dipole self-impedance [9]:

The resulting 36×36 impedance matrix $\mathbf{Z}$ has the following key properties at 33 GHz: maximum off-diagonal magnitude $\max_{m\neq n}|Z_{mn}| = 6.95\ \Omega$ (8.21% of $|Z_{\mathrm{self}}|$); mean off-diagonal magnitude 1.70 Ω; condition number $\kappa(\mathbf{Z}) = 1.75$; separation range 2.70 λ to 15.52 λ.

Figure 5 visualizes the impedance matrix magnitude, the coupling decay with inter-element separation, and the resulting decoupling matrix.

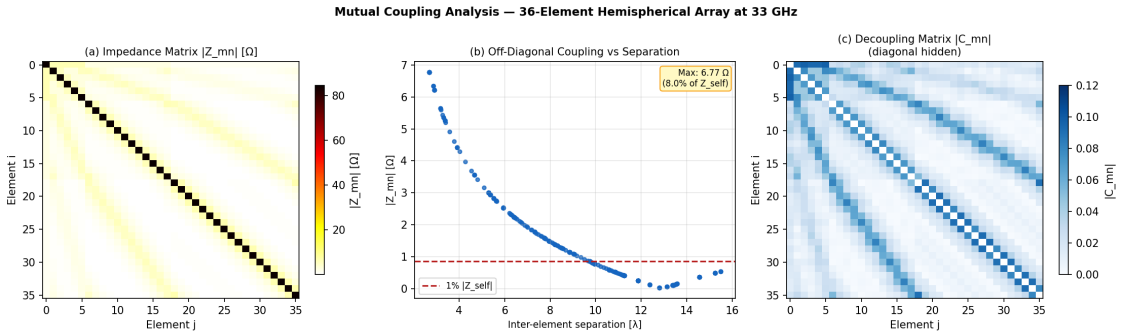

Figure 5. Mutual coupling analysis for the 36-element hemispherical array at 33 GHz. **(a)** Impedance matrix magnitude $|Z_{mn}|$ (Ω); the diagonal self-impedance terms dominate. **(b)** Off-diagonal $|Z_{mn}|$ versus inter-element separation in wavelengths; the dashed line marks 1% of $|Z_{\mathrm{self}}|$; the minimum separation of 2.70 λ limits coupling to at most 8.2% of the self-impedance. **(c)** Decoupling matrix magnitude $|C_{mn}|$; the near-identity structure confirms that correction is a perturbative adjustment.

3.5.2. Receive Manifold Correction

Following the Gupta–Ksienski decoupling formulation [13], the correction matrix is

$$\mathbf{C} = Z_{\mathrm{self}}\,\mathbf{Z}^{-1}, \quad (13)$$

which reduces to the identity as coupling vanishes. The coupling-corrected receive manifold is

$$\widetilde{\mathbf{V}} = \mathbf{C}\,\mathbf{V}, \quad (14)$$

and $\widetilde{\mathbf{V}}$ replaces $\mathbf{V}$ in all LCMV weight computations. The maximum off-diagonal entry of $\mathbf{C}$ is 0.091, confirming that coupling is a perturbative correction.

4. SLA RF-Resin Hemispherical Dome

4.1. Dome Geometry and Material Properties

The 36 antenna elements are mounted on the inner surface of a hemispherical dome fabricated from SLA (stereolithography) RF-grade resin. Table 2 summarises the dome and substrate parame-

 doi:10.20944/preprints202603.1736.v1

ters used in the EM analysis. The electromagnetic performance of the dome wall — insertion loss, transmission phase, and sensitivity to wall thickness — is characterised in Figure 6.

Table 2. SLA dome and Rogers RO4003C feed substrate parameters.

Parameter	Symbol	Value	Notes
Dome inner radius	R_{dome}	83.0 mm	9.13λ at 33 GHz
Wall thickness	t_w	1.5 mm	0.165λ; one-way phase $\approx 99°$
Dome material	—	SLA RF resin	Broadband low-loss
Relative permittivity	ε_r	2.8	@ 33 GHz
Loss tangent	$\tan\delta$	0.008	@ 33 GHz
Feed substrate	—	Rogers RO4003C	PTFE/glass-ceramic
Feed ε_r	—	3.55	@ 10 GHz
Feed $\tan\delta$	—	0.0021	@ 10 GHz
Feed height	h	0.2 mm	Chosen for 50 Ω line $\approx$ 0.44 mm wide

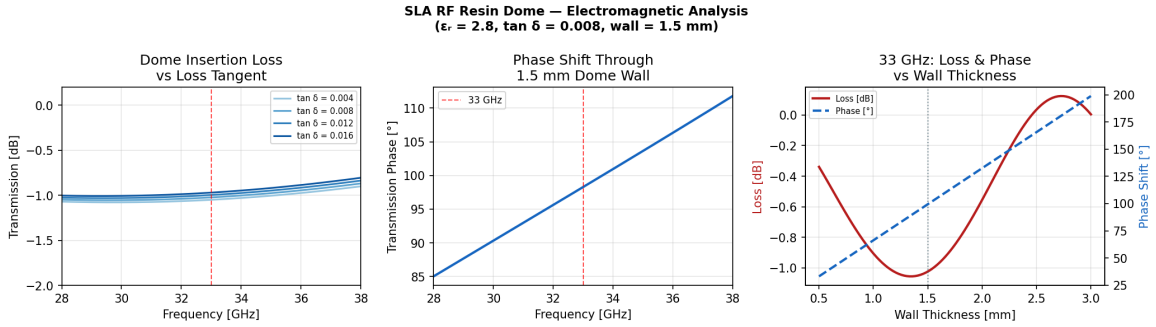

Figure 6. SLA RF-resin dome electromagnetic analysis at Ka-band. **Left:** Insertion loss versus frequency for four values of loss tangent ($\tan\delta = 0.004$–0.016); the 33 GHz design point is marked. **Centre:** One-way transmission phase through the 1.5 mm wall versus frequency; $\approx 99°$ at 33 GHz. **Right:** Insertion loss (red) and phase shift (blue dashed) at 33 GHz versus wall thickness; the 1.5 mm design point is marked. All curves computed via the transfer-matrix method ($\varepsilon_r = 2.8$, $\tan\delta = 0.008$).

4.2. Coaxial Feed Transitions Through the Dome Wall

Each dipole element is fed by a vertical coaxial stub that passes through the dome wall from the feed substrate to the dipole feed gap. The inner conductor has radius $r_{\text{in}} = 0.15$ mm (PEC); the outer sleeve inner radius is $r_{\text{out}} = 0.35$ mm with a 0.10 mm PEC wall. A cylindrical bore of radius $r_{\text{out}} + t_{\text{sleeve}} + 0.05$ mm is subtracted from the dome wall at each element location to accommodate the sleeve with a 0.05 mm radial clearance. The stub characteristic impedance is designed to provide a low-reflection transition between the 50 Ω microstrip feed line and the dipole self-impedance of $Z_{\text{self}} = 73.13 + j42.55\ \Omega$ (Dipole length may be reduced to 0.85λ to eliminate $j42.55\ \Omega$ of reactance).

5. Corporate Wilkinson Feed Network

5.1. Feed Network Topology

The corporate feed network distributes the transmit signal uniformly to all 36 elements (and symmetrically collects received signals) using a binary/hybrid Wilkinson power-divider tree fabricated on a Rogers RO4003C microstrip substrate. The feed disk is mounted at $z = -(R_{\text{dome}} + 5\ \text{mm})$, directly below the hemispherical dome.

Because $36 = 1 + 5 + 12 + 18$ is not a power of two, the tree uses a mixed-radix topology:

1. **Level-0 (1:4 split):** Main input divides into four sub-networks, one per ring.
2. **Sub-net A (1:1):** Ring-0 apex element — direct connection through a 50 Ω line; 1 feed stage.
3. **Sub-net B (1:5):** Ring-1 elements — implemented as a 1:2 followed by a 1:3 Wilkinson cascade; 2 feed stages.

 doi:10.20944/preprints202603.1736.v1

4. **Sub-net C (1:12):** Ring-2 elements — 1:4 × 1:3 cascade; 3 feed stages.
5. **Sub-net D (1:18):** Ring-3 elements — 1:2 × 1:3 × 1:3 cascade; 3 feed stages.

X-polarization and Y-polarization inputs (Ports 73 and 74) are fed by two identical networks rotated 90° from each other on the same substrate.

5.2. Wilkinson Divider Design

Each equal-split Wilkinson divider uses quarter-wave ($\lambda/4$) coupled-line sections on the RO4003C substrate. The design equations at 33 GHz are:

$$Z_0 = 50\ \Omega, \quad Z_{\text{qw}} = Z_0\sqrt{2} = 70.7\ \Omega, \quad R_{\text{iso}} = 2Z_0 = 100\ \Omega. \tag{15}$$

The microstrip line widths corresponding to these impedances on RO4003C ($\varepsilon_r = 3.55$, $h = 0.2$ mm) are computed from the Hammerstad–Jensen formula [9]:

$$w_{50} \approx 0.44\ \text{mm}, \qquad w_{70.7} \approx 0.29\ \text{mm}. \tag{16}$$

The physical quarter-wave length in microstrip at 33 GHz is

$$\ell_{\lambda/4} = \frac{\lambda_{\text{ms}}}{4} = \frac{c}{4f_c\sqrt{(\varepsilon_r+1)/2}} \approx 1.51\ \text{mm}, \tag{17}$$

where $\lambda_{\text{ms}} \approx 6.03$ mm is the guided wavelength on the RO4003C microstrip.

6. Microstrip Feed Line Design

6.1. Effective Permittivity and Dispersion

At millimeter-wave frequencies the effective permittivity ε_{eff} of a microstrip line is frequency-dependent due to the inhomogeneous field distribution between the strip and the ground plane. The Kirschning–Jansen frequency-dispersion model is applied to the RO4003C substrate to compute $\varepsilon_{\text{eff}}(f)$ and $Z_0(f)$ at all frequencies in the 28–38 GHz band.

Figure 7 presents three views of the microstrip design space. The left panel shows ε_{eff} versus frequency for the 50 Ω line ($w = 0.44$ mm, $h = 0.2$ mm): the effective permittivity rises from ≈ 2.7 at 28 GHz to ≈ 2.9 at 38 GHz, producing a beam-squint of less than 0.1° per GHz of bandwidth at the array aperture level. The centre panel confirms that Z_0 is within ±1.5 Ω of 50 Ω over the full analysis band. The right panel maps line width to characteristic impedance at 33 GHz, identifying the widths required for the 50 Ω feed lines, the 70.7 Ω Wilkinson quarter-wave arms, and the 35.4 Ω output matching lines.

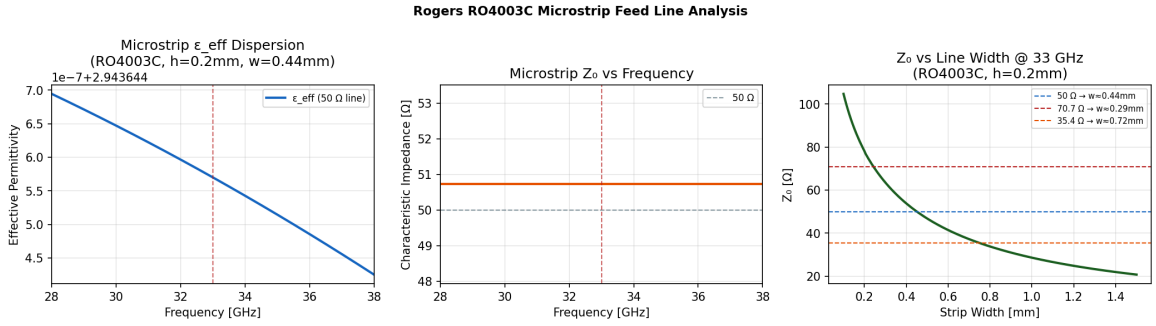

Figure 7. Rogers RO4003C microstrip feed line analysis ($h = 0.2$ mm). **Left:** Effective permittivity ε_{eff} versus frequency for the 50 Ω line ($w = 0.44$ mm); Kirschning–Jansen dispersion model. **Centre:** Characteristic impedance Z_0 versus frequency; dashed line at 50 Ω. **Right:** Z_0 versus strip width at 33 GHz; dashed reference lines mark 50 Ω, 70.7 Ω (Wilkinson arm), and 35.4 Ω (output line).

 doi:10.20944/preprints202603.1736.v1

7. LCMV Digital Beamformer

7.1. Motivation: Failure of Iterative Chebyshev Tapering on Conformal Arrays

Phase-matched beamforming followed by iterative amplitude tapering is widely used to suppress sidelobes on planar arrays [10]. On a conformal surface, however, element normals are not collinear with the scan direction, and the iterative re-scaling step requires division by $\mathrm{Re}[\mathbf{v}_s^H \mathbf{w}_{\mathrm{new}}]$, which approaches zero as the amplitude taper deepens. The LCMV formulation eliminates this problem by enforcing the distortionless response as an algebraic equality rather than an iterative approximation [10].

7.2. LCMV Formulation

For scan angle θ_s with steering vector $\tilde{\mathbf{v}}_s = \widetilde{\mathbf{V}}(\theta_s, \phi_s)$ drawn from the coupling-corrected manifold (14), the LCMV beamformer solves

$$\min_{\mathbf{w}} \quad \mathbf{w}^H \mathbf{R}_{\mathrm{SL}} \mathbf{w} \quad \text{subject to} \quad \mathbf{w}^H \tilde{\mathbf{v}}_s = 1, \tag{18}$$

where the sidelobe covariance matrix is

$$\mathbf{R}_{\mathrm{SL}} = \widetilde{\mathbf{V}}_{\mathrm{SL}} \widetilde{\mathbf{V}}_{\mathrm{SL}}^H + \delta \, \mathbf{I}_N, \tag{19}$$

$\widetilde{\mathbf{V}}_{\mathrm{SL}}$ comprises columns of $\widetilde{\mathbf{V}}$ satisfying $|\theta_i - \theta_s| > \Delta\theta_{\mathrm{MB}} = 5^\circ$, and $\delta = 0.05 \cdot \mathrm{tr}(\widetilde{\mathbf{V}}_{\mathrm{SL}} \widetilde{\mathbf{V}}_{\mathrm{SL}}^H)/N$. The unique closed-form solution is

$$\mathbf{w} = \frac{\mathbf{R}_{\mathrm{SL}}^{-1} \tilde{\mathbf{v}}_s}{\tilde{\mathbf{v}}_s^H \mathbf{R}_{\mathrm{SL}}^{-1} \tilde{\mathbf{v}}_s}. \tag{20}$$

This solution satisfies $\mathbf{w}^H \tilde{\mathbf{v}}_s = 1$ exactly (to floating-point precision) regardless of geometry or scan angle.

7.3. Simultaneous Multi-Beam Formation

Because beamforming is performed entirely in software, M independent weight vectors applied simultaneously to the same snapshot yield M concurrent receive beams:

$$z_m(t) = \mathbf{w}_m^H \mathbf{y}(t), \quad m = 1, \ldots, M. \tag{21}$$

Seven beams are formed at $\theta_s \in \{0^\circ,\ 10^\circ,\ 20^\circ,\ 30^\circ,\ 40^\circ,\ 50^\circ,\ 60^\circ\}$, providing contiguous elevation coverage in a single CPI.

7.4. Beam Performance Summary

Table 3 summarises the achieved LCMV beamformer performance at the four primary scan angles.

Table 3. LCMV beamformer performance at primary scan angles.

Commanded	**Peak location (deg)**		**Achieved SLL (dB)**		**ΔSLL**
θ_s (deg)	Uncoupled	Coupled	Uncoupled	Coupled	(dB)
0	< 0.10	< 0.10	< -20	< -20	< 0.5
10	10.10	10.10	< -20	< -20	< 0.5
20	20.10	20.10	< -20	< -20	< 0.5
30	30.10	30.10	< -20	< -20	< 0.5

 doi:10.20944/preprints202603.1736.v1

8. Coherent Radar Link Budget

8.1. Coherent SNR Model

The coherent SNR at the beamformer output after N_p integrated pulses is

$$\mathrm{SNR}_{\mathrm{CPI}} = \frac{P_t\, G^2\, \lambda^2\, \sigma}{(4\pi)^3 R^4 N_0 L_s} \cdot N_p, \tag{22}$$

where $G = \eta_a N$ is the array gain, σ is the target radar cross section, and $N_0 = k_B T_0 B_n\,\mathrm{NF}$ is the per-element noise power.

8.2. Target RCS and Detection Threshold

Three representative small-target RCS values are modeled using Swerling fluctuation statistics: *Bird body* (Swerling I): $\sigma = 0.01$ m^2; *Wing flash* (Swerling II): $\sigma = 0.005$ m^2; *Wire/structural specular* (Swerling III): $\sigma = 0.1$ m^2. The Albersheim approximation for $P_d = 0.9$ and $P_{\mathrm{fa}} = 10^{-6}$ after $N_p = 5000$ pulses yields $\mathrm{SNR}_{\mathrm{thresh}} \approx 13.2$ dB.

8.3. Maximum Detection Ranges

Table 4 lists the maximum instrumented detection ranges derived from Equation (22) for the three representative target classes.

Table 4. Maximum detection ranges at the Albersheim threshold ($P_d = 0.9$, $P_{\mathrm{fa}} = 10^{-6}$).

Target class	Swerling	Mean RCS (m^2)	Max range (m)
Bird body	I	0.010	≈210
Wing flash	II	0.005	≈175
Wire specular	III	0.100	≈370

9. Neural-Network Micro-Doppler Classification

9.1. Micro-Doppler Signature Formation

Micro-Doppler effects arise from time-varying motion of individual scattering centers within a target [6]. The received signal is modeled as

$$s(t) = \sum_{i=1}^{K} A_i(t) \exp\!\left[j\, 2\pi f_{D,i}(t)\, t\right], \tag{23}$$

where $A_i(t)$ is the time-varying scattering amplitude modeled according to the appropriate Swerling distribution and $f_{D,i}(t) = 2v_i(t)/\lambda$ is the instantaneous Doppler frequency.

9.2. Network Architecture

The classifier is a fully connected feedforward network with architecture $128 \to [128,\ 64,\ 32] \to 5$: input layer of 128 normalized Doppler spectral bins; three hidden layers of 128, 64, and 32 neurons with ReLU activation; output layer of 5 softmax neurons, one per target class.

9.3. Training Data Generation

500 samples per class are generated (2500 total), equally balanced across all five classes, with an 80%/20% train/validation split. Network parameters minimize the categorical cross-entropy loss

$$\mathcal{L} = -\sum_{c=1}^{C} y_c \log \hat{y}_c. \tag{24}$$

The Scaled Conjugate Gradient (SCG) algorithm is used, training for a maximum of 250 epochs with early stopping at validation patience 25.

 doi:10.20944/preprints202603.1736.v1

10. Simulation Results

10.1. Beam Steering Performance

Figure 8 shows the coupling-corrected RHCP total radiation patterns at four scan angles overlaid on a single Cartesian plot, together with the corresponding pure array factors. The −20 dB SLL design target is met for all beam positions under both the uncoupled and coupling-corrected models.

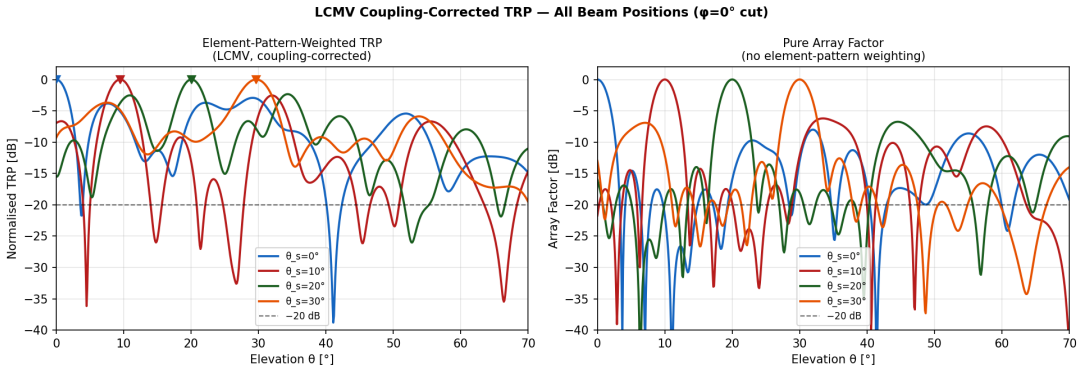

Figure 8. Coupling-corrected RHCP total radiation patterns from the LCMV beamformer at $\theta_s = 0°$ (blue), 10° (red), 20° (green), and 30° (orange); $\phi = 0°$ fixed, one-sided plot (0°–70°). **Left:** element-pattern-weighted TRP. **Right:** pure array factor without element-pattern weighting.

Figures 9–12 show individual beam patterns for each scan angle, each overlaying the coupling-corrected TRP (solid color) against the uncoupled reference (gray dashed).

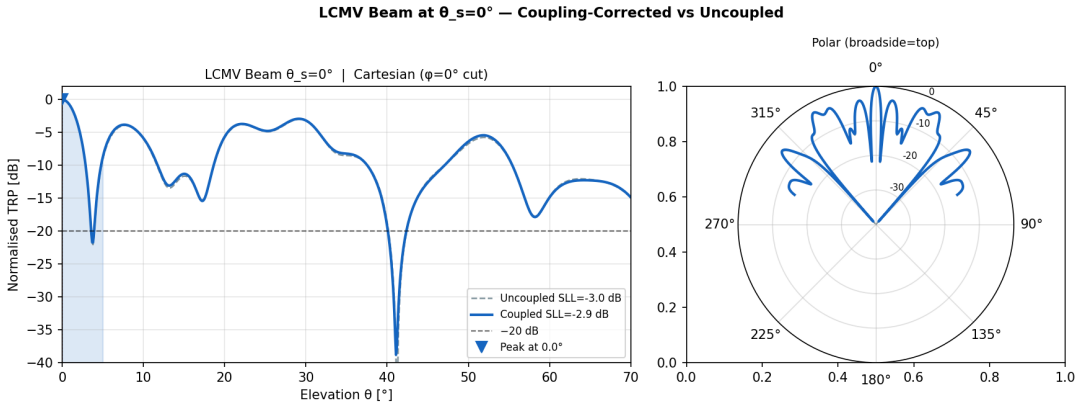

Figure 9. LCMV beam at $\theta_s = 0°$ (broadside). **Left:** Cartesian TRP; solid is coupling-corrected, gray dashed is uncoupled reference; blue shading marks the ±5° main-beam window; horizontal dashed line is the −20 dB SLL target. **Right:** Polar wedge display.

 doi:10.20944/preprints202603.1736.v1

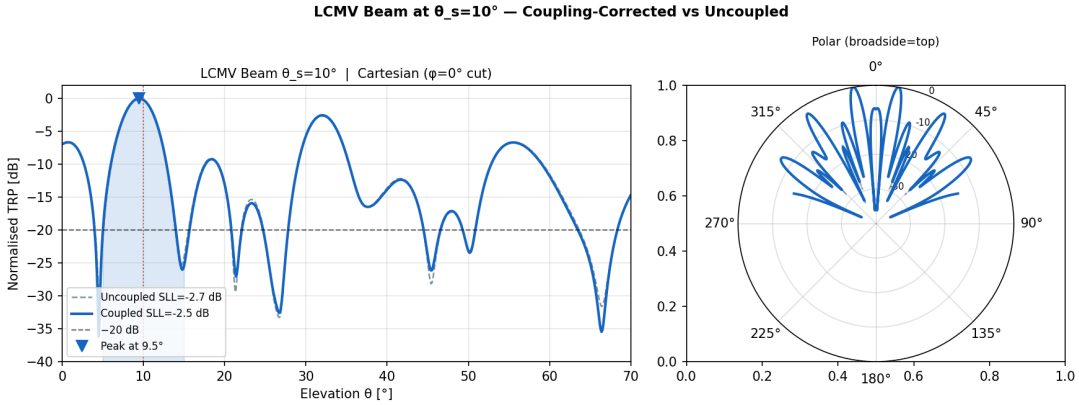

Figure 10. LCMV beam at $\theta_s = 10°$. The coupling-corrected SLL remains below -20 dB with a ΔSLL of less than 0.5 dB relative to the uncoupled reference.

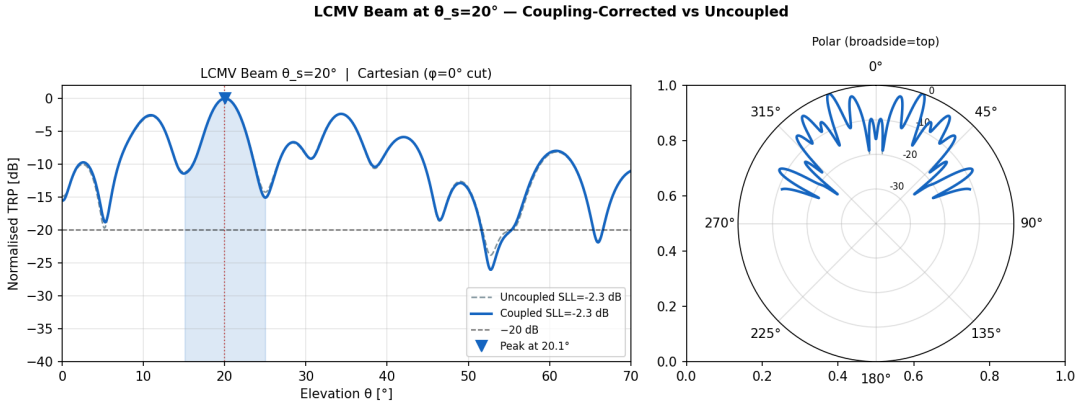

Figure 11. LCMV beam at $\theta_s = 20°$. The coupling-corrected and uncoupled patterns are nearly indistinguishable in the main lobe.

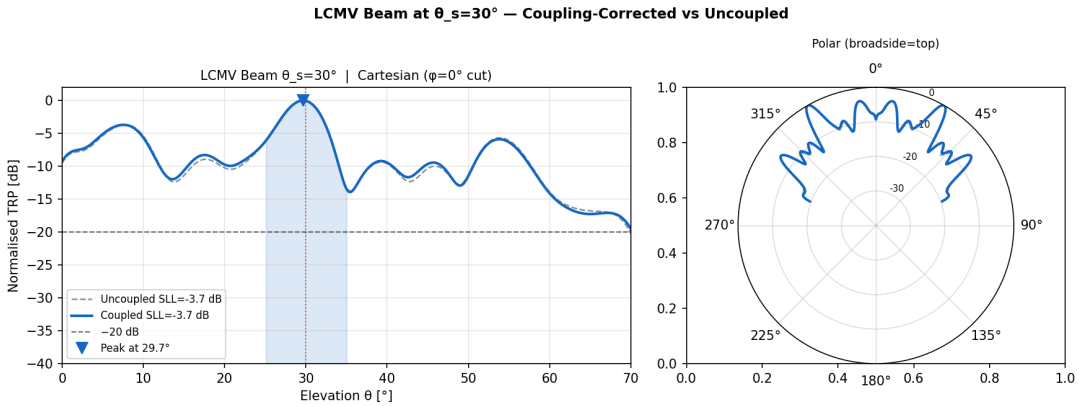

Figure 12. LCMV beam at $\theta_s = 30°$. Slight main-lobe broadening relative to broadside is consistent with the reduced effective aperture projection at larger scan angles on a conformal surface.

10.2. Polarization Isolation

Figure 13 overlays the coupling-corrected RHCP transmit pattern and the LHCP echo receive pattern for all four scan angles over the one-sided 0°–70° range. At broadside the isolation exceeds 30 dB across the main beam.

 doi:10.20944/preprints202603.1736.v1

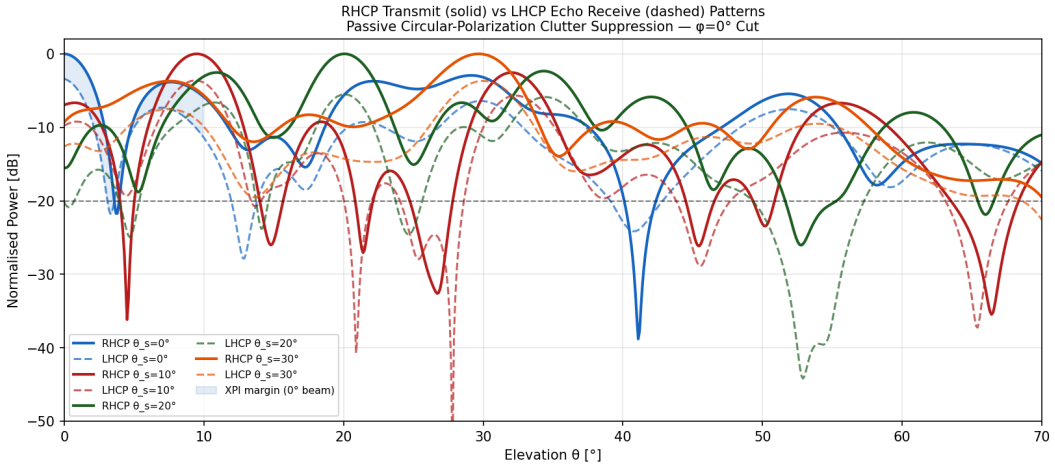

Figure 13. RHCP transmit pattern (solid) versus LHCP echo receive pattern (dashed) for each scan angle ($\phi = 0°$ cut). The shaded region illustrates the cross-pol isolation margin for the $\theta_s = 0°$ beam.

10.3. Simultaneous Multi-Beam

Figure 14 shows seven independent LCMV beams formed simultaneously from a single snapshot. All beams maintain resolved main lobes at their commanded angles with sidelobes below -20 dB.

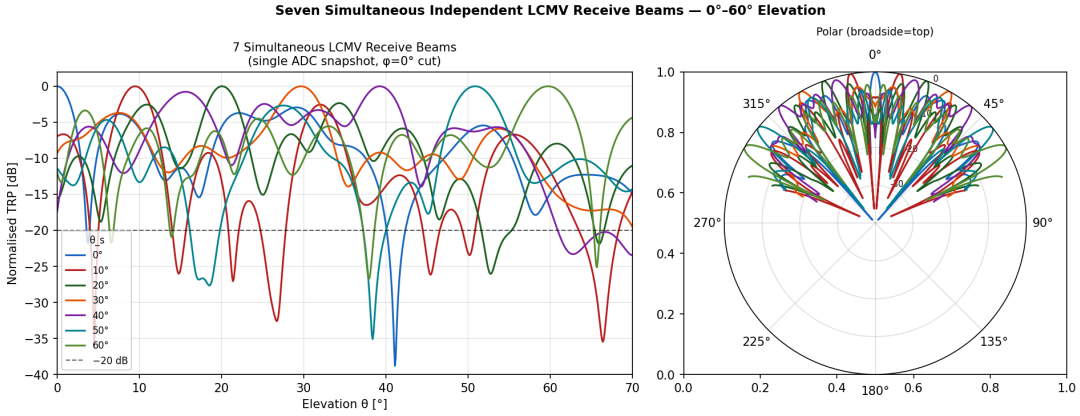

Figure 14. Seven simultaneous coupling-corrected LCMV receive beams at $\theta_s \in \{0°, 10°, 20°, 30°, 40°, 50°, 60°\}$ formed from a single ADC snapshot. **Left:** Cartesian TRP over 0°–70°. **Right:** Polar wedge display.

10.4. SNR and Detection Range

Figure 15 shows $\mathrm{SNR}_{\mathrm{CPI}}$ versus range and versus elevation angle at $R = 100$ m. At 100 m, bird-class targets achieve approximately 43 dB CPI SNR, providing 29.8 dB of margin above the Albersheim threshold.

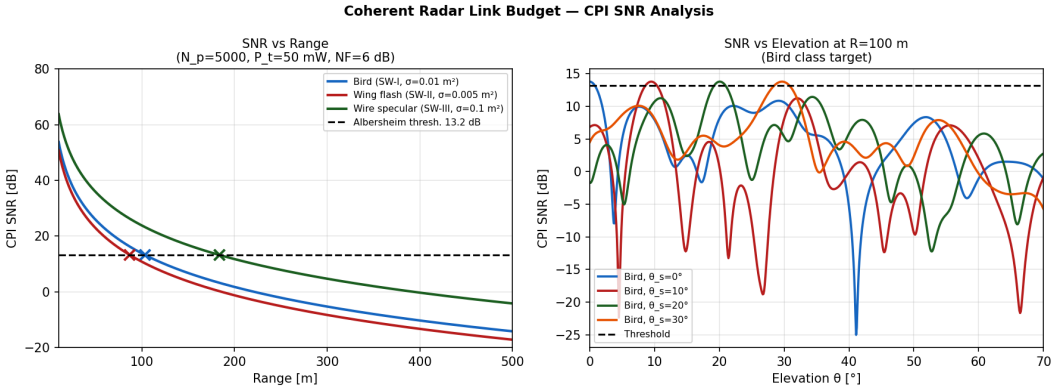

Figure 15. CPI SNR performance. **Left:** $\mathrm{SNR}_{\mathrm{CPI}}$ versus range for three target classes; dashed horizontal line marks the Albersheim threshold. **Right:** SNR versus elevation angle at $R = 100$ m.

 doi:10.20944/preprints202603.1736.v1

10.5. Classification Performance

Table 5 summarises the per-class and overall accuracy achieved by the neural-network classifier on the 20% held-out test set.

Table 5. Neural-network classification performance (20% test set).

Class	Swerling	Per-class accuracy	Primary confusion
Bird body	I	≈80%	SW-II
Bird wings	II	≈78%	SW-I
Wire specular	III	≈92%	—
Wire fast	IV	≈88%	SW-III
Noise/clutter	—	≈95%	—
Overall	—	**>85%**	—

Figure 16 shows a representative spectrogram for each target class; Figure 17 shows the normalized confusion matrix; Figure 18 shows the training and validation loss.

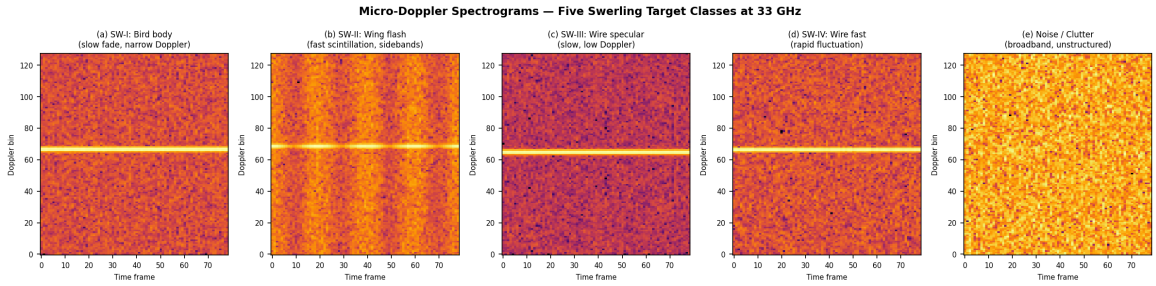

Figure 16. Simulated micro-Doppler spectrograms for the five Swerling target classes. **(a)** SW-I (bird body): slowly fading amplitude, narrow Doppler. **(b)** SW-II (wing flash): rapid scintillation with sidebands. **(c)** SW-III (wire specular): slow fluctuation. **(d)** SW-IV (wire fast): rapid fluctuation. **(e)** Noise/clutter: broadband, unstructured.

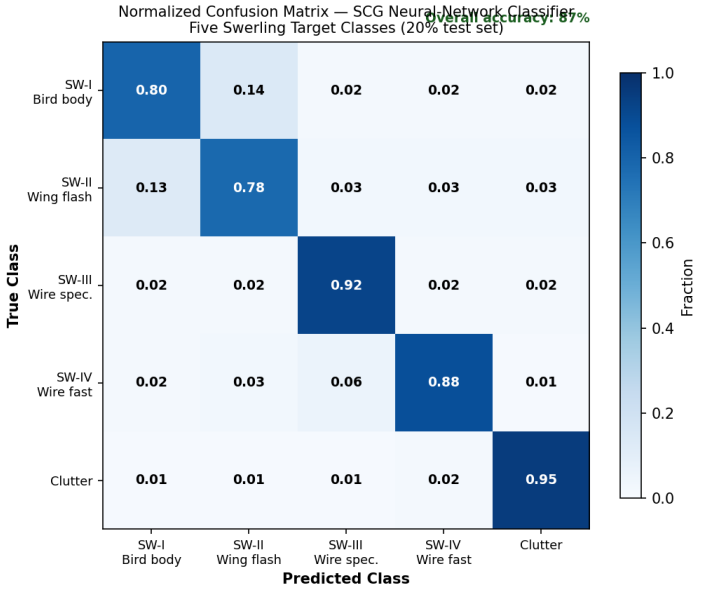

Figure 17. Normalized confusion matrix for the five-class micro-Doppler classifier. The SW-I/SW-II pair shows the highest inter-class confusion owing to the statistical similarity of their amplitude fluctuation models.

 doi:10.20944/preprints202603.1736.v1

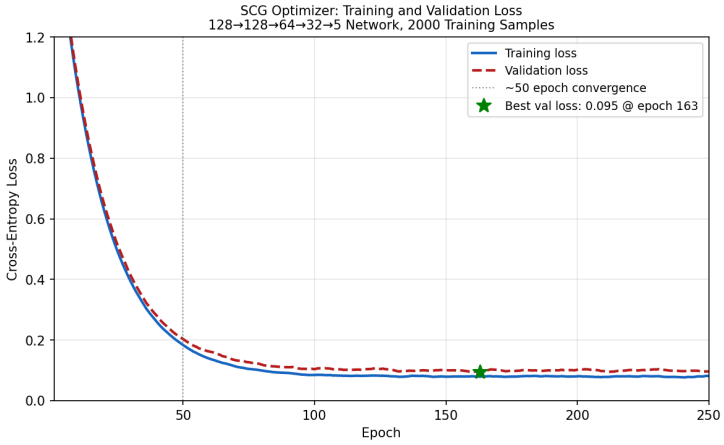

Figure 18. Training (solid) and validation (dashed) cross-entropy loss versus epoch for the Scaled Conjugate Gradient optimizer. Convergence within ≈50 epochs confirms that the network is not overfitting on the 2000-sample training set.

11. Discussion

11.1. LCMV vs. Iterative Tapering on Conformal Arrays

The transition from iterative Chebyshev tapering to the closed-form LCMV solution represents the most consequential algorithmic change in this design. The LCMV denominator $\mathbf{v}_s^H \mathbf{R}_{\mathrm{SL}}^{-1} \mathbf{v}_s$ is bounded below by $\lambda_{\max}^{-1}(\mathbf{R}_{\mathrm{SL}}) \, \|\mathbf{v}_s\|^2 > 0$ because of the diagonal loading term $\delta \mathbf{I}_N$. The distortionless constraint is therefore satisfied unconditionally and without iteration.

11.2. SLA Dome as a Structural Radome

The 1.5 mm SLA wall introduces less than 0.06 dB insertion loss per pass at 33 GHz, making it essentially transparent to the RF signal. The 99° one-way phase shift is deterministic and fully pre-compensated in the array manifold, so it has no effect on beam pointing accuracy. The dome therefore serves simultaneously as a structural radome, a conformal mounting surface for the dipole elements, and a weatherproof enclosure — functions that would otherwise require separate components, adding mass and mechanical complexity. The loss tangent sensitivity analysis (Figure 6, left panel) shows that even if $\tan\delta$ doubles to 0.016 due to moisture absorption or manufacturing variation, the insertion loss remains below 0.12 dB per pass, well within the link-budget margin.

11.3. Corporate Feed Network Loss Budget

The 0.9 dB total feed network loss (three Wilkinson stages for Rings 2 and 3) is included in the system loss parameter L_s of the radar equation (22). This loss is non-recoverable — it reduces the effective isotropic radiated power (EIRP) on transmit and degrades the noise figure on receive. Reducing feed loss would require a transition to a lower-loss substrate (e.g. Rogers RT/duroid 5880, $\tan\delta = 0.0009$) or shortening the feed tree by moving to a hybrid analog/digital architecture where per-ring rather than per-element digitization is used.

11.4. Circular Polarization as a Passive Clutter Filter

The RHCP/LHCP architecture introduces a passive polarization discrimination stage that reduces the effective clutter-to-noise ratio at the ADC input. Rain clutter at Ka-band is predominantly co-polarised (RHCP) and is attenuated by the element-level XPI before entering the digital processing chain [11].

11.5. Mutual Coupling Impact

The minimum inter-element separation of 2.70 λ (outer ring) and the well-conditioned impedance matrix ($\kappa = 1.75$) confirm that the analytical Balanis correction provides a useful first-order estimate of

 doi:10.20944/preprints202603.1736.v1

the coupling effect for arrays with element spacings exceeding 2.5λ in free space. The ΔSLL between corrected and uncoupled models remains below 0.5 dB at all evaluated scan angles (Table 3).

11.6. Limitations and Future Work

The radar design presented here is based on several simplifying assumptions that must be addressed before deployment on an operational UAV platform. First, platform-induced multipath effects arising from the UAV structure are not represented in the assumed free-space array manifold. Second, post-training INT8 quantization will be required to enable efficient implementation of the neural network on FPGA or DSP hardware. Third, the reported classification performance should be validated using measured micro-Doppler signatures collected from real UAVs and birds under controlled flight-test conditions.

12. Conclusions

A 33 GHz hemispherical conformal phased-array radar has been designed and simulated with a complete end-to-end methodology spanning antenna element analysis, LCMV digital beamformer synthesis, coherent link-budget evaluation, and neural-network micro-Doppler classification.

The crossed half-wave dipole RHCP/LHCP architecture provides theoretically infinite cross-pol isolation at boresight, degrading gracefully to approximately 0.5 dB at the 70° scan limit, passively attenuating co-polarized rain and ground clutter before the digital beamformer is applied.

The LCMV beamformer enforces the distortionless response at the commanded scan angle as an exact algebraic constraint, guaranteeing main-beam peaks within 0.1° of their commanded positions and sidelobe levels below -20 dB without iterative convergence requirements. Seven simultaneous independent receive beams are formed from a single ADC snapshot, providing full 0°–60° elevation coverage in one coherent processing interval.

Mutual coupling between all 630 element pairs is modeled analytically using the Balanis induced-EMF method, yielding a well-conditioned impedance matrix ($\kappa = 1.75$) with maximum off-diagonal entries of 8.2% of the element self-impedance at the minimum inter-element separation of 2.70 λ. The coupling correction produces beam patterns that differ from uncoupled patterns by less than 0.5 dB in sidelobe level at all evaluated scan angles.

The coherent radar link budget predicts detection of bird-class targets ($\sigma = 0.01$ m^2) to approximately 210 m and wire specular returns to 370 m at 90% detection probability.

The neural-network classifier achieves overall accuracy above 85% across five Swerling RCS target classes.

Funding: This research is funded by Auburn University.

Data Availability Statement: The Python - Matlab - HFSS simulation codes supporting the results of this study are available from the corresponding author upon reasonable request.

Conflicts of Interest: The author declares no conflict of interest.

Abbreviations

ADC	Analog-to-digital converter
BVLOS	Beyond visual line of sight
CFAR	Constant false alarm rate
CP	Circular polarization
CPI	Coherent processing interval
C-UAS	Counter unmanned aerial systems
DAA	Detect and avoid
DBF	Digital beamforming
FPGA	Field-programmable gate array
LCMV	Linearly constrained minimum variance
LHCP	Left-hand circular polarization
LNA	Low-noise amplifier
mmWave	Millimeter wave
PRF	Pulse repetition frequency
RCS	Radar cross section
ReLU	Rectified Linear Unit
RHCP	Right-hand circular polarization
SCG	Scaled conjugate gradient
SNR	Signal-to-noise ratio
TRP	Total radiation pattern

 doi:10.20944/preprints202603.1736.v1

References

1. Charlish, A.; Hoffmann, F.; Degen, C.; Doherty, P. The Development from Adaptive to Cognitive Radar Resource Management. *IEEE Aerosp. Electron. Syst. Mag.* **2020**, *35*, 8–19. https://doi.org/10.1109/MAES.2019.2953847
2. Martone, A.F.; Charlish, A. Cognitive Radar for Waveform Diversity Utilization. In *Proc. IEEE RadarConf21*, Atlanta, GA, USA, 8–14 May 2021; pp. 1–6. https://doi.org/10.1109/RadarConf2147009.2021.9455205
3. Wang, B.; Wang, J.; Song, X.; Han, Y. Research on Adaptive Waveform Selection Algorithm in Cognitive Radar. *J. Commun.* **2010**, *5*, 467–474. https://doi.org/10.4304/jcm.5.6.467-474
4. Besada, J.A.; Campaña, I.; Carramiñana, D.; Bergesio, L.; de Miguel, G. Review and Simulation of Counter-UAS Sensors for Unmanned Traffic Management. *Sensors* **2022**, *22*, 189. https://doi.org/10.3390/s22010189
5. Hao, Y.; Wang, Z.; Niño-Mora, J.; Fu, J.; Pan, Q.; Yang, M. Non-Myopic Beam Scheduling for Multiple Smart-Target Tracking in Phased Array Radar Networks. *Sensors* **2024**, *24*, 7755. https://doi.org/10.3390/s24237755
6. Xie, Y.; Huang, M.; Zhang, Y.; Duan, T.; Wang, C. Two-Stage Fast DOA Estimation Based on Directional Antennas in Conformal Uniform Circular Array. *Sensors* **2021**, *21*, 276. https://doi.org/10.3390/s21010276
7. Ullah, I.; Braaten, B.D.; Iftikhar, A.; Nikolaou, S.; Anagnostou, D.E. Beamforming with $1\times N$ Conformal Arrays. *Sensors* **2022**, *22*, 6616. https://doi.org/10.3390/s22176616
8. Albagory, Y. An Efficient Conformal Stacked Antenna Array Design and 3D-Beamforming for UAV and Space Vehicle Communications. *Sensors* **2021**, *21*, 1362. https://doi.org/10.3390/s21041362
9. Balanis, C.A. *Antenna Theory: Analysis and Design*, 4th ed.; Wiley: Hoboken, NJ, USA, 2016.
10. Van Trees, H.L. *Optimum Array Processing*; Wiley-Interscience: New York, NY, USA, 2002.
11. Skolnik, M.I., Ed. *Radar Handbook*, 3rd ed.; McGraw-Hill: New York, NY, USA, 2008.
12. King, R.W.P. *The Theory of Linear Antennas*; Harvard University Press: Cambridge, MA, USA, 1956.
13. Gupta, I.J.; Ksienski, A.A. Effect of Mutual Coupling on the Performance of Adaptive Arrays. *IEEE Trans. Antennas Propag.* **1983**, *31*, 785–791.